

# CLUSTERING BY DENOISING: LATENT PLUG-AND-PLAY DIFFUSION FOR SINGLE-CELL DATA

**Dominik Meier**  
Cornell Tech  
dm954@cornell.edu

**Shixing Yu**  
Cornell Tech  
sy774@cornell.edu

**Sagnik Nandy**  
Ohio State University  
nandy.15@osu.edu

**Promit Ghosal**  
University of Chicago  
promit@uchicago.edu

**Kyra Gan**  
Cornell Tech  
kyragan@cornell.edu

## ABSTRACT

Single-cell RNA sequencing (scRNA-seq) enables the study of cellular heterogeneity. Yet, clustering accuracy, and with it downstream analyses based on cell labels, remain challenging due to measurement noise and biological variability. In standard latent spaces (e.g., obtained through PCA), data from different cell types can be projected close together, making accurate clustering difficult. We introduce a *latent plug-and-play diffusion* framework that *separates the observation and denoising space*. This separation is operationalized through a novel Gibbs sampling procedure: the learned diffusion prior is applied in a low-dimensional latent space to perform denoising, while to steer this process, noise is *reintroduced into the original high-dimensional observation space*. This unique “input-space steering” ensures the denoising trajectory remains faithful to the original data structure. Our approach offers three key advantages: (1) *adaptive noise handling* via a tunable balance between prior and observed data; (2) *uncertainty quantification* through principled uncertainty estimates for downstream analysis; and (3) *generalizable denoising* by leveraging clean reference data to denoise noisier datasets, and via averaging, *improve quality beyond the training set*. We evaluate robustness on both synthetic and real single-cell genomics data. Our method improves clustering accuracy on synthetic data across varied noise levels and dataset shifts. On real-world single-cell data, our method demonstrates improved biological coherence in the resulting cell clusters, with cluster boundaries that better align with known cell type markers and developmental trajectories.

## 1 INTRODUCTION

Single-cell RNA sequencing (scRNA-seq) has revolutionized biomedical research by enabling high-resolution profiling of cellular heterogeneity (Park et al., 2020; Miragaia et al., 2019), with large-scale initiatives like the Human Cell Atlas providing foundational references for *cell type annotation* (Regev et al., 2017; Lindeboom et al., 2021; Elmentaite et al., 2022; Stuart et al., 2019; Lopez et al., 2018). However, since cells are sequenced without predefined labels, accurate cell type identification must be derived entirely from unsupervised analysis of noisy high-dimensional data. The canonical approach involves reducing dimensionality (e.g., via PCA) followed by clustering and manual annotation based on marker genes—an iterative and subjective process (Kiselev et al., 2019; Stuart et al., 2019). This paradigm suffers from three major limitations: 1) scRNA-seq data is inherently noisy due to technical artifacts (e.g., varying capture efficiency, Kharchenko et al. 2014) and biological stochasticity (Wagner et al., 2016), which clustering algorithms amplify, often producing unreliable labels; 2) Reproducibility is hampered by batch effects and procedural differences across labs (Shaham et al., 2017), making consistent clustering across datasets difficult; and 3) Population-specific and technology-induced shifts in data distribution reduce generalizability.

We frame single-cell denoising as an inverse problem: recovering clean gene expression from noisy measurements without imposing strong generative assumptions. This follows the *plug-and-play* (PnP) paradigm (Venkatakrisnan et al., 2013a; Zhang et al., 2021; Chan et al., 2016; Ryu et al.,

2019), which integrates powerful denoising priors with measurement models. Mainstream PnP diffusion frameworks (Zhu et al., 2023; Go et al., 2023; Wu et al., 2024; Xu & Chi, 2024) enables this through combining likelihoods via iterative refinement (e.g., Gibbs sampling), where each denoising step is followed by controlled noise reintroduction to enforce data consistency. In principle, this enables denoising beyond test data quality by transferring patterns from high-signal reference data (e.g., SMART-seq2, Picelli et al. 2013; 2014) to noisier technologies (e.g., droplet-based scRNA-seq, Klein et al. 2015; Macosko et al. 2015). However, directly applying image-based PnP frameworks to single-cell data is challenging. Unlike images where pixel noise is largely independent, gene expression data exhibits intrinsic low-rank structure and complex correlations. Moreover, denoising must preserve relational structure between cells for accurate clustering and annotation. Standard dimensionality reduction (e.g., PCA) can collapse distinct cell types, making it impossible to guide denoising accurately.

To address these unique challenges, we introduce a *latent plug-and-play diffusion framework* that tailors the PnP philosophy to single-cell biology. Unlike prior PnP methods that rely on generic or hand-designed priors, our approach is tailored to biological data and operates through a *modified two-step procedure*, designed to overcome limitations of prior single-cell denoising methods. *First*, a diffusion model is trained in a low-dimensional latent space (analogous to PCA) to capture the core biological manifold of a *high-quality reference dataset*. Unlike PCA, this diffusion process learns score functions directly from the data, enabling recovery of complex structures in the latent distribution of cell types. This approach inherits the robustness to prior misspecification and scalability to high latent dimensions characteristic of diffusion models (Xu & Chi, 2024). *Second*, during inference on the *noisy dataset*, we employ a *Gibbs sampling procedure that reintroduces noise into the original high-dimensional input space*. This critical step directly addresses the *latent-space collapsing issue* inherent in methods like PCA (Burges et al., 2010), where distinct biological states are projected too close together, losing information essential for precise denoising. By operating in the original high-dimensional space, where full geometric relationships are preserved, our method steers denoising toward biologically meaningful structures obscured in compressed representations.

Our framework diverges from existing Bayesian approaches for single-cell analysis by removing their need for restrictive generative modeling. While variational autoencoders (VAEs) (Lopez et al., 2018; Gayoso et al., 2019; Grønbech et al., 2020) are difficult to train and rely on strong likelihood assumptions, more recent *approximate message passing* methods with empirical Bayes denoisers (Zhong et al., 2022; Nandy & Ma, 2024) still require parametric noise modeling, operate purely in the latent space, and scale poorly to high-dimensional latent spaces. In contrast, our approach requires no explicit generative model or pre-processing for noise structure, instead learning it directly from data. By combining the adaptability of likelihood-free diffusion with the structure-aware refinement of Gibbs-based input-space guidance, we enhance cluster separation even under high noise or distribution shift, without depending on restrictive architectural or noise-modeling priors.

Our framework offers three key advantages over existing single-cell clustering and denoising methods, providing a principled, robust, and reproducible pathway for automated cell type annotation:

- **Adaptive noise handling through tunable interpolation:** We introduce a parameter  $\rho$  that dynamically balances data-driven information and prior knowledge during denoising. This allows optimal adaptation to varying noise levels and dataset qualities—preserving data-specific signals when test and training distributions align, while leveraging prior knowledge to stabilize highly noisy inputs. This capability is absent in conventional clustering and imputation methods.
- **Uncertainty quantification:** Unlike standard clustering or VAE-based pipelines, our approach provides confidence sets for cell-type predictions, enabling quantitative assessment of annotation reliability—critical for downstream analysis and clinical applications.
- **Generalizable denoising:** By training on high-quality reference data, our model learns a robust biological manifold that can denoise even low-quality target datasets, effectively addressing real-world scenarios where data from different labs exhibit substantial quality variations. Further, our averaging-based approach enables denoising beyond the immediate training distribution, enhancing applicability across diverse experimental conditions.

Our experimental results demonstrate consistent performance under various mis-specifications of the data-generating process in synthetic settings (Section 4). In real-world single-cell experiments, our method shows strong potential for leveraging high-signal training data to improve denoising in low-signal datasets and to denoise beyond the training distribution by averaging (Section 5).

**Additional Related Work on Diffusion in Single-Cell Data** Diffusion models provide flexible, trainable priors that accommodate complex noise structures (Sohl-Dickstein et al., 2015; Ho et al., 2020; Song et al., 2021b;a). While initial single-cell applications have focused on transcriptome generation and data imputation (Luo et al., 2024; Wang et al., 2025; 2024; Zhang et al., 2025), their potential for learning denoised low-dimensional embeddings, critical for reference atlas construction and robust label transfer, remains largely unexplored beyond restrictive generative modelling assumptions. Our work investigates this gap, using unsupervised clustering and subsequent biological validation as the evaluation framework.

## 2 SINGLE-CELL ATLAS CONSTRUCTION VIA POSTERIOR SAMPLING

We consider two single-cell RNA-seq datasets: (1) a reference dataset  $\mathcal{D}^{(r)} = \{X_1^{(r)}, \dots, X_m^{(r)}\}$  used to train a diffusion prior that captures the underlying biological manifold, and (2) a target dataset  $\mathcal{D}^{(t)} = \{X_1^{(t)}, \dots, X_n^{(t)}\}$  to which we apply denoising using the learned prior. Both datasets consist of raw UMI counts transformed into expression profiles via standard preprocessing pipelines (e.g., quality control, variance stabilization, etc.). Our framework is agnostic to specific preprocessing choices and accommodates diverse noise structures.

**Data Generating Process** We assume both datasets follow a low-rank factor model (Peng et al., 2021; Weine et al., 2024; Zhong et al., 2022; Nandy & Ma, 2024; Argelaguet et al., 2020). Let  $X_i \in \mathbb{R}^d$ :

$$X_i = VU_i + \varepsilon_i, \quad \forall i, \quad (1)$$

where  $V \in \mathbb{R}^{d \times k}$  is a factor loading matrix that spans the transcriptional space;  $U_i \in \mathbb{R}^k \sim P_{\text{prior}}$  encodes the low-dimensional *biological cell signal* drawn i.i.d. from an *unknown* distribution  $P_{\text{prior}}$ ; and  $\varepsilon_i$  is an independent noise vector, reflecting stochastic variation in the measurement process or biological stochasticity. For specific datasets, we have

$$X^{(r)} = U^{(r)} \left( V^{(r)} \right)^\top + \varepsilon^{(r)}, \quad U^{(r)} \in \mathbb{R}^{m \times k}, \quad \varepsilon^{(r)} \in \mathbb{R}^{m \times d}, \quad (2)$$

$$X^{(t)} = U^{(t)} \left( V^{(t)} \right)^\top + \varepsilon^{(t)}, \quad U^{(t)} \in \mathbb{R}^{n \times k}, \quad \varepsilon^{(t)} \in \mathbb{R}^{n \times d}. \quad (3)$$

We assume conserved latent biological structures across datasets: the prior distribution  $P_{\text{prior}}$  (shared cell state manifold) and factor loading matrix  $V$  (transcriptional programs) are identical for both reference and target datasets. However, we allow dataset-specific noise characteristics  $\varepsilon^{(t)} \approx \varepsilon^{(r)}$  to accommodate different measurement technologies and batch effects, *with the expectation that our method performs best when the reference dataset  $\mathcal{D}^{(r)}$  has comparable or lower noise levels than the target dataset  $\mathcal{D}^{(t)}$ .*

Given these shared structures, we drop superscripts on  $U$  and  $V$  entirely, as they represent the same biological quantities across datasets. We retain the  $(r)$  and  $(t)$  superscripts only for dataset-specific terms:  $\mathcal{D}^{(r)}$ ,  $\mathcal{D}^{(t)}$ ,  $X^{(r)}$ ,  $X^{(t)}$ ,  $\varepsilon^{(r)}$ , and  $\varepsilon^{(t)}$ . To further simplify notation, we henceforth drop the superscripts with the convention that all quantities refer to the target dataset  $\mathcal{D}^{(t)}$  unless explicitly marked with  $(r)$  for the reference dataset  $\mathcal{D}^{(r)}$ .

**Posterior Sampling for Denoised Embeddings** Our goal is to construct a *denoised atlas* of  $\mathcal{D}^{(t)}$  by computing posterior embeddings  $\mathbb{E}[U_i | X_i]$ , which we frame as sampling from the posterior:

$$\pi(U | X) \propto f(X - UV^\top | U) P_{\text{prior}}(U),$$

where  $f(\cdot)$  denotes the likelihood associated with the observation model, and  $P_{\text{prior}}$  represents the population prior learned via diffusion on  $\mathcal{D}^{(r)}$ . The main challenge lies in the likelihood term  $f(X - UV^\top | U)$ , which encodes the relationship between latent embeddings and observed expressions through the factor model in Eq. (1). Traditional approaches address this difficulty by imposing restrictive assumptions: conjugate Gaussian priors with Gaussian likelihoods (Gelman et al., 2013) enable tractable inference but fail to capture complex biological distributions, while Metropolis-adjusted Langevin algorithms (Roberts & Rosenthal, 1998; Durmus et al., 2018) handle non-Gaussian likelihoods but struggle with implicitly defined diffusion priors.

**PnP Framework with Auxiliary Variables** By leveraging the PnP diffusion framework, we overcome this challenge using a *split Gibbs sampling* approach (Xu & Chi, 2024) that introduces auxiliary variables  $Z_i$  to decouple the likelihood from the diffusion prior. This is achieved by first

replacing  $U_i$  with  $Z_i$  in the likelihood generating stage, and then enforce consistency between  $U_i$  and  $Z_i$  through a Gaussian penalty, which leads to following augmented joint distribution:

$$P_\rho(X_i, U_i, Z_i) \propto \exp\left(-\log f(X_i - VZ_i) - \frac{1}{2\rho^2}\|U_i - Z_i\|_2^2 - \log P_{\text{prior}}(U_i)\right), \quad (4)$$

where  $\rho$  controls the alignment strength. Smaller  $\rho$  enforces tighter coupling between  $U_i$  and its auxiliary counterpart  $Z_i$ . This leads to a Gibbs sampler alternating between two conditional updates:

$$\textbf{Likelihood Step: } P_\rho(Z_i | X_i, U_i) \propto \exp\left(-\log f(X_i - VZ_i) - \frac{1}{2\rho^2}\|U_i - Z_i\|_2^2\right), \quad (5)$$

$$\textbf{Prior Step: } P_\rho(U_i | Z_i) \propto \exp\left(-\frac{1}{2\rho^2}\|U_i - Z_i\|_2^2 - \log P_{\text{prior}}(U_i)\right). \quad (6)$$

Although resembling Gibbs sampling, the alignment penalty is *artificially introduced* rather than arising from standard conjugacy. This modification allows us to plug in a diffusion prior at inference time, thereby enabling efficient posterior sampling even when the prior is only implicitly specified.

**Evaluating Atlas Quality** A key challenge in single-cell atlas construction is the lack of direct evaluation metrics due to high-dimensional noise and the curse of dimensionality (Kiselev et al., 2019). We employ a multi-faceted evaluation strategy combining quantitative clustering metrics and qualitative visual assessment:

1. *Visual Assessment:* We use dimensionality reduction techniques, particularly UMAP (McInnes et al., 2018), to visually examine the quality of denoised embeddings. Well-separated, biologically meaningful structures in 2D visualizations validate the method’s performance.
2. *Unsupervised Clustering with Post-Hoc Evaluation:* Denoised embeddings  $\{\widehat{U}_i\}_{i=1}^n$  are clustered without using label information to obtain  $K$  clusters. The quality of these clusters is evaluated by comparing them to the known cell type labels  $L_i \in 1, \dots, C$  using metrics like *adjusted rand index* (ARI) (Hubert & Arabie, 1985), average silhouette score (Rousseeuw, 1987), and cell-type Locally Invariant Simpson Index (Korsunsky et al., 2019), which quantify the agreement between the data-driven clusters and biological annotations.

Our framework is fully unsupervised, relying only on expression data.<sup>1</sup> We benchmark performance on synthetic data with known ground truth and on real datasets, noting that real-world labels may be imperfect (and thus annotation accuracy thus provides an indirect measure of atlas quality).

### 3 METHOD

We introduce a *latent plug-and-play diffusion scheme* for denoising query cell embeddings under the guidance of a diffusion model trained on a large corpus of single-cell gene expression data. Leveraging the PnP framework, we recover low-dimensional embeddings  $U$  from noisy gene expression profiles  $X^{(r)}$  by *decoupling data fidelity and prior structure*: the query cell’s expression profile anchors the denoising process to its unique features, while the pretrained diffusion model contributes global information about the structure of the cell population. Our pipeline consists of two stages:

1. **Training stage:** jointly estimate the factor loading matrix  $V$  and train a diffusion model to learn the prior distribution  $P_{\text{prior}}$  over embeddings on  $\mathcal{D}^{(r)}$ .
2. **Inference stage:** given query expressions  $X_q^{(t)}$ , perform posterior sampling using a split Gibbs scheme, alternating between likelihood-informed updates and diffusion-guided updates.

This approach preserves the flexibility of diffusion priors while maintaining tractable posterior inference, providing a scalable and uncertainty-aware framework for single-cell atlas construction.

**Diffusion Training** We train the diffusion model on the reference dataset  $\mathcal{D}^{(r)}$ . Consider the best rank- $k$  approximation of the reference data produced by singular value decomposition:  $X^{(r)} \approx \widehat{W}\widehat{\Sigma}\widehat{V}^\top$ , where  $\widehat{W} \in \mathbb{R}^{n \times k}$  and  $\widehat{V} \in \mathbb{R}^{d \times k}$  are unitary matrices containing the top  $k$  left and right singular vectors, respectively, and  $\widehat{\Sigma} \in \mathbb{R}^{k \times k}$  is the diagonal matrix of the top  $k$  singular values. This decomposition yields our loading matrix estimate in Eq. (1),  $\widehat{V}$ . We then compute the transformed

<sup>1</sup>While labels are not used in denoising, we explore label-augmented diffusion training in Section 5.

---

**Algorithm 1** DICE: Diffusion Induced Cell Embeddings

---

- 1: **Input:** query cell  $X_q$ ; trained diffusion model  $\hat{\epsilon}_{\theta_t}(\cdot)$ ; number of iterations  $T$ ; annealing schedule  $\{\rho_s\}_{s=1}^T$ ; estimated factor loading matrix  $\hat{V}$
  - 2: **Initialize:**  $U_q^{(0)} \leftarrow \hat{V}^\top X_q$
  - 3: **for**  $s = 0$  to  $T - 1$  **do**
  - 4:   **Likelihood alignment:** sample
$$Z_q^{(s)} \mid U_q^{(s)} \propto \exp\left(-\frac{1}{2\rho_s^2}\|Z_q - U_q^{(s)}\|_2^2 - \log f(X_q - \hat{V}Z_q)\right).$$
  - 5:   **Prior alignment:** Using the reverse diffusion update in Eq. (7), sample
$$U_q^{(s+1)} \mid Z_q^{(s)} \propto \exp\left(-\frac{1}{2\rho_s^2}\|Z_q^{(s)} - U_q\|_2^2 - \log P_{\text{prior}}(U_q)\right).$$
  - 6: **end for**
  - 7: **return**  $U_q^{(T)}$  as the denoised embedding of the query cell.
- 

observations  $\hat{U}_i = \hat{V}^\top X_i^{(r)}$  for  $i = 1, \dots, m$ , which accurately approximates the latent embeddings  $U_i$  under a wide range of noise models. These estimated embeddings  $\{\hat{U}_i\}_{i=1}^m$  therefore provide approximate training samples from the prior distribution  $P_{\text{prior}}$  and are used to train the diffusion model.

To learn this prior, we adopt the standard forward-diffusion framework (Sohl-Dickstein et al., 2015; Ho et al., 2020), which we detail in Appendix A.

**Denosing with DICE** We now introduce DICE (Diffusion Induced Cell Embeddings, Algorithm 1), our split Gibbs sampling procedure for denoising a query cell  $X_q$  and estimating its latent embedding  $U_q$ . Given an annealing schedule  $\{\rho_s : s = 1, \dots, T\}$ , the augmented distribution Eq. (4) decomposes posterior sampling into two iterative steps:

1. **Likelihood alignment** (Line 4) is implemented using either a general proximal scheme (Xu & Chi, 2024) or a closed-form Gaussian update when  $f$  is Gaussian (Proposition 3.1). Unlike the likelihood alignment step in Eq. (5), Line 4 operates in the original  $d$ -dimensional data space, reintroducing noise through the likelihood function  $\log f(X_q - \hat{V}Z_q)$ .
2. **Prior alignment** (Line 5) is implemented using the trained diffusion model via the reverse update

$$x_{t-1} = \frac{1}{\sqrt{\alpha_t}} \left( x_t - \frac{1 - \alpha_t}{\sqrt{1 - \alpha_t}} \hat{\epsilon}_\theta(x_t) \right) + \sqrt{1 - \alpha_t} z_t, \quad z_t \sim \mathcal{N}(0, I_k), \quad (7)$$

run for  $t = t_0, t_0 - 1, \dots, 1$  with initialization  $x_{t_0} = \sqrt{\bar{\alpha}_{t_0}} U_q^{(s)}$ . The chain length is chosen so that  $\bar{\alpha}_{t_0} \approx (1 + \rho_s^2)^{-1}$ .

We reduce posterior variability by generating multiple samples and averaging, enabling denoising beyond reference data quality (Figure 1 (first column) and Figure 3). The parameter  $\rho_s$  controls the relative weight of prior and likelihood: a larger  $\rho_s$  emphasizes population-level structure and is suitable for noisy queries, while a smaller  $\rho_s$  emphasizes fidelity to the observed expression profile.

**Likelihood Alignment under Gaussian Noise** Although our framework accommodates general likelihoods, in practice, single-cell data are often  $\log 1p$ -transformed and modeled with Gaussian noise (Zhong et al., 2022; Argelaguet et al., 2020). In this case, Proposition 3.1 (proof in Appendix B) establishes that the likelihood update step admits a closed-form update:

**Proposition 3.1.** *Assume  $f$  is the standard multivariate Gaussian density in  $d$  dimensions. Following Gaussian conjugacy, for all  $s = 0, \dots, T - 1$ , the likelihood update step (Line 4) admits the following update:*

$$Z_q^{(s)} \sim \mathcal{N}\left(\Lambda \left( \hat{V}^\top X_q + \frac{1}{\rho_s^2} U_q^{(s)} \right), \Lambda\right), \quad \Lambda = \left( \hat{V}^\top \hat{V} + \frac{1}{\rho_s^2} I_k \right)^{-1}.$$

**Remark 3.2.** *The same denoising scheme can be applied to the training data themselves, yielding refined embeddings that serve as a reference atlas. Notably, atlas construction via DICE does not rely on restrictive parametric assumptions for either the likelihood or the prior, enabling the method to capture rich and complex population structures as found for example in single-cell data.*

**Confidence Sets** We quantify uncertainty in the embedding of a query cell  $X_q$  by applying DICE multiple times and examining the spread of the resulting denoised embeddings.

## 4 EVALUATION ON SYNTHETIC DATA

**Setup** To evaluate how well DICE recovers clean latent structure from noisy expression profiles, we design a controlled setting that mimics two *pure* cell populations with known labels. In latent dimension  $k = 15$ , the training prior is a balanced Gaussian mixture  $P_{\text{prior}} = \frac{1}{2} \mathcal{N}_{15}(0_{15}, 1.5 I_{15}) + \frac{1}{2} \mathcal{N}_{15}(1_{15}, 1.3 I_{15})$ , with each component corresponding to one cell type. We sample a loading matrix  $V \in \mathbb{R}^{2000 \times 15}$  with entries i.i.d.  $\mathcal{N}(0, 1)$ . For each cell  $i$ , we draw a latent  $U_i^{(r)} \sim P_{\text{prior}}$  and measurement noise  $\varepsilon_i^{(r)} \sim \mathcal{N}_{2000}(0, I_{2000})$ , and generate a synthetic expression profile  $X_i^{(r)} = VU_i^{(r)} + \varepsilon_i^{(r)} \in \mathbb{R}^{2000}$ ,  $i = 1, \dots, 1600$ . This yields a reference dataset  $\mathcal{D}^{(r)}$  of size  $m = 1600$  in  $d = 2000$  observed dimensions, analogous to a high-signal scRNA-seq experiment with two subpopulations present in equal proportion.

**Test configurations** We examine three train-test shifts covering practical single-cell scenarios, with  $|\mathcal{D}^{(t)}| = 400$ , fixing  $P_{\text{prior}}$  and  $V$  as in Section 2 unless noted otherwise:

1. **Setup 1 (matched train–test distribution).** We generate  $\mathcal{D}^{(t)}$  from the same DGP as  $\mathcal{D}^{(r)}$  to isolate posterior denoising effects. This evaluates whether DICE improves population separation in latent space versus PCA, mirroring standard atlas workflows where query cells are mapped via denoised embeddings (Nandy & Ma, 2024).
2. **Setup 2 (signal-strength shift).** We increase the noise on  $\mathcal{D}^{(t)}$ , with  $\varepsilon_i^{(t)} \sim \mathcal{N}_{2000}(0, 10 I_{2000})$ . This mirrors single-cell scenarios with lower read depth/fewer UMIs or noisier platforms (e.g., shallow sequencing) that reduce *signal-to-noise ratio* (SNR) at test time. This tests whether DICE, trained on high-quality data, denoises low-SNR profiles better than PCA.
3. **Setup 3 (noise-model shift).** We generate  $\mathcal{D}^{(t)}$  with a heavy-tailed noise,  $\varepsilon_i^{(t)} \sim \mathfrak{t}_{\nu=4}(I_{2000})$  (multivariate  $\mathfrak{t}$  with 4 degrees of freedom and scale  $I_{2000}$ ), while keeping a Gaussian likelihood during denoising. This tests DICE’s robustness to likelihood mis-specification from heavy-tailed residuals (due to outliers, doublets, or over-dispersion in single-cell applications) against PCA.
4. **Setup 4 (latent-prior shift).** We change the test latent distribution to a heavy-tailed mixture:  $U_i^{(t)} \stackrel{\text{i.i.d.}}{\sim} \frac{1}{2} \mathcal{N}_{15}(1_{15}, 1.5 I_{15}) + \frac{1}{2} \mathfrak{t}_{\nu=4}(1.3 I_{15})$ , with increased noise  $\varepsilon_i^{(t)} \sim \mathcal{N}_{2000}(0, 10 I_{2000})$ . This tests robustness to prior mis-specification when deploying on novel, heterogeneous subpopulations (e.g., new developmental states), where we expect DICE to recover mixture separation better than PCA despite heavier tails and lower SNR.

**Training and denoising workflow** We train a diffusion model on 15-dimensional latent representations obtained via PCA from the training set  $\mathcal{D}^{(r)}$  for 2,000 epochs (training details in Appendix C). The resulting model serves as the learned prior  $P_{\text{prior}}$  across all four test configurations.

At test time, we denoise the PCA projections of each configuration by running Algorithm 1 (DICE) for  $T = 200$  Gibbs iterations with a constant annealing level  $\rho_t = 20$ . We repeat this procedure with 10 independent random iterations and report the mean of the resulting embeddings as a Monte Carlo estimate of  $\mathbb{E}[U | X]$  for each test cell.

**Evaluation** We assess the cluster separation of DICE-derived embeddings against a PCA baseline that projects expression profiles to the same latent dimension used for clustering. Qualitatively, we visualize UMAPs (McInnes et al., 2018) (Fig. 1); quantitatively, we report the average *cosine* silhouette score (Rousseeuw, 1987), computed using the true cluster labels of the test data (Table 1). Because ground-truth labels are available in this benchmark, both readouts are directly comparable. Across all four settings, DICE yields clearer separation in UMAP and higher silhouette scores than the PCA baseline, indicating more faithful recovery of the underlying classes.

**Uncertainty in the embeddings** We visualize our confidence set construction for two fixed points: (i) the center of Cluster 2 and (ii) the midpoint between the two cluster centers. For each input, we run DICE 500 times and project the resulting embeddings onto the same UMAP as the training data. When the input lies at the center of a cluster (Figure 2, left), all embeddings map consistently to Cluster 2, indicating high confidence in the cluster assignment. In contrast, when the input lies between clusters (Figure 2, right), the embeddings are split across both clusters, reflecting uncertainty in the assignment. Such uncertainty could be advantageous for downstream tasks designed to incorporate soft labels. Additional plots in subsection E.1 show how the parameter  $\rho$  directly controls the size of the confidence sets. Thus,  $\rho$  must be tuned to balance coverage and performance.

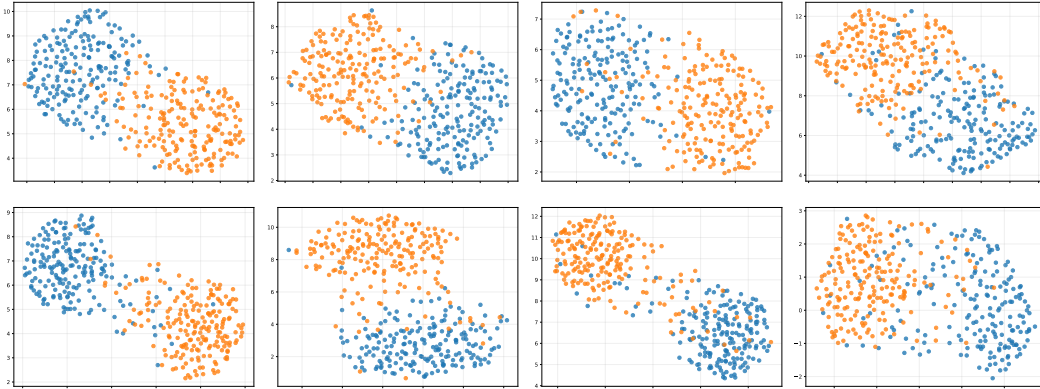
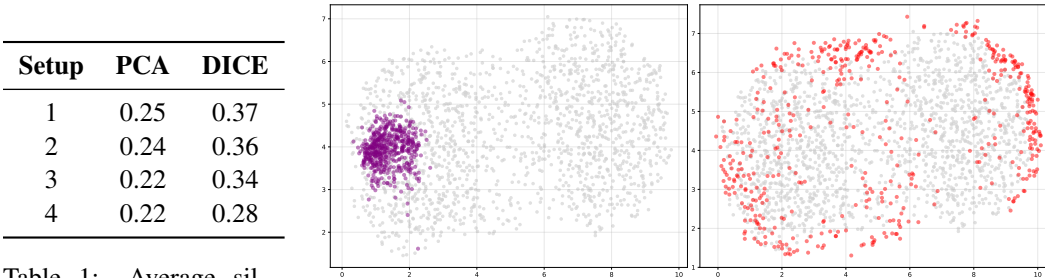


Figure 1: UMAP visualizations of the 400 test cells for each of the four configurations. Top row: PCA projections; bottom row: DICE-denoised embeddings. Columns (left to right) correspond to Setups 1–4. Throughout, we refer to the mixture component centered at  $1_{15}$  with scale  $1.3 I_{15}$  as **Cluster 1**, and to the complementary component as **Cluster 2** (Gaussian  $\mathcal{N}_{15}(0_{15}, 1.5 I_{15})$  where applicable; heavy-tailed  $\tau_{\nu=4}(1.3 I_{15})$  in the latent–prior–shift configuration). Points are colored blue for **Cluster 1** and orange for **Cluster 2**.



Setup	PCA	DICE
1	0.25	0.37
2	0.24	0.36
3	0.22	0.34
4	0.22	0.28

Table 1: Average silhouette scores (higher is better) for two methods across four settings.

Figure 2: UMAP visualizations of 500 runs of DICE on the same input point in Setup 1 and  $\rho = 0.1$ . Training data are shown in grey. Left: center of Cluster 2; Right: midpoint between Clusters 1 and 2.

## 5 EVALUATION ON SINGLE-CELL DATA

We evaluate the effectiveness of DICE in denoising single-cell gene expression profiles using two publicly available single-cell RNA-seq datasets: the CITE-seq dataset from [Hao et al. \(2021\)](#) and the *human fetal brain development* datasets from [Polioudakis et al. \(2019\)](#) and [Nowakowski et al. \(2017\)](#). These datasets originate from distinct tissues and capture diverse cellular populations. They also differ in their relative signal strengths, allowing us to examine the ability of our method to handle both complex cell distributions and varying signal-to-noise regimes.

**Diffusion Training** For each dataset, we first select the latent dimension  $k$  using the elbow of the singular-value spectrum, and then project the training data onto this  $k$ -dimensional space via PCA. This yields the training embeddings  $\{\hat{U}_i\}_{i=1}^m$  and the loading matrix  $\hat{V}$  used by DICE. We train the same diffusion architecture across datasets using AdamW with a cosine-annealed learning-rate schedule. Additional details on the training pipeline, including precise model architecture, are provided in Section C of the appendix.

### 5.1 ANALYSIS OF THE CITE-SEQ DATASET

**Dataset** CITE-seq dataset ([Hao et al., 2021](#)) consists of RNA profiles for 20,729 genes across 152,094 PBMCs with paired *antibody-derived tags* (ADT) measurements. We focus solely on the transcriptomic modality and uniformly subsample 10,000 cells for analysis. Ground-truth labels are provided, and we adopt the  $L2$ -level granularity, which distinguishes  $\sim 30$  immune subtypes.

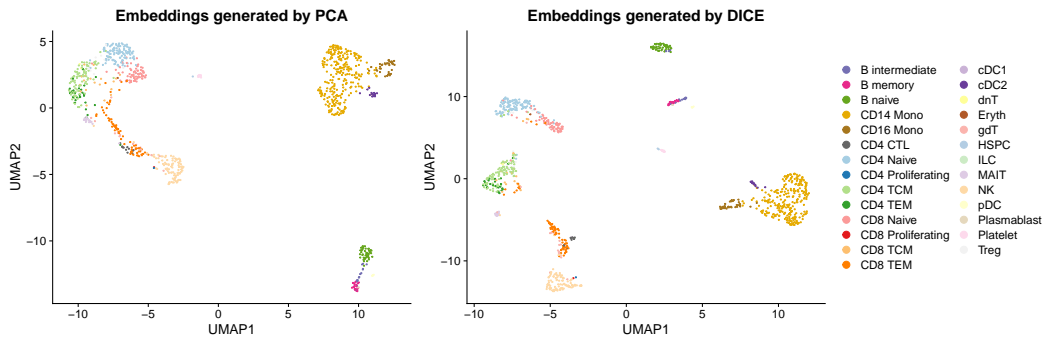


Figure 3: UMAP of 1,000 held-out PBMCs from the CITE-seq dataset. Left: PCA embeddings in a 25-dimensional latent space using  $\hat{V}$  from the training set. Right: embeddings after denoising with DICE using a diffusion model trained on the other 9,000 cells.

**Preprocessing and denoising** We applied standard QC, removing cells with  $< 200$  genes, genes expressed in  $< 3$  cells, and cells with  $> 15\%$  mitochondrial counts. Using library size factors computed from the dataset, we normalized counts to  $10^4$  per cell, followed by  $\log(1+x)$  transformation to stabilize variance. We selected the top 3,000 highly variable genes (Seurat v3 criterion), scaled to unit variance with values capped at 10. Batch effects from sequencing lanes were corrected with Harmony (Korsunsky et al., 2019), yielding a matrix  $X \in \mathbb{R}^{10000 \times 3000}$ . We split into 9,000 training and 1,000 held-out test cells with preserved label proportions. Similar to **Setup 1**, we test DICE’s ability in denoising beyond the quality of the training dataset in this setting. The training set was used to fit the diffusion model, and the test set was reserved for evaluation.

Using the training pipeline above, we picked  $k = 25$  and trained a diffusion model on 25d PCA embeddings and applied DICE for  $T = 100$  denoising iterations to the PCA embeddings of the test cells. We used a linearly decreasing (equally spaced) annealing schedule  $\{\rho_t\}_{t=1}^T$  from 5 to 0.5 over 100 points. Further details of the denoising procedure are provided in [Appendix C](#).

**Evaluation** We compare UMAP (McInnes et al., 2020) visualizations of the 1,000 held-out test cells denoised by DICE against their PCA projections without denoising (Figure 3). Denoised embeddings show clearer segregation of immune subtypes, with marked improvement in separating sub lineages of CD4 and CD8 T cells. The DICE atlas also performs better in segregating the MAIT cells from the other T cells. These populations are notoriously difficult to resolve from RNA alone (Hao et al., 2021), a challenge that originally motivated multimodal approaches combining RNA and protein. In the unimodal setting considered here, however, popular toolkits such as Seurat rely directly on PCA embeddings. Our results indicate that denoising PCA embeddings with priors learned from high-signal training data substantially improves cluster separation, supporting more reliable annotation of held-out cells. Beyond visual inspection, we also quantify clustering quality using the Adjusted Rand Index (ARI) (Hubert & Arabie, 1985) computed after Leiden clustering on a 20-nearest-neighbor graph built from the embeddings, comparing recovered clusters to the true cell labels provided in the metadata. The PCA-based embeddings achieve an ARI of 0.7165, whereas the DICE embeddings achieve 0.7563, illustrating the effectiveness of our approach in better segregating distinct cell populations.

## 5.2 ANALYSIS OF HUMAN FETAL BRAIN DEVELOPMENT DATASETS

**Datasets** We evaluate the effectiveness of DICE in transferring cell type information learned from high-signal training data to related low-signal test data using scRNA-seq datasets from Nowakowski et al. (2017) and Polioudakis et al. (2019). Both datasets profile human fetal brain tissue during development. The Nowakowski et al. (2017) dataset includes cells from primary cortical and *medial ganglionic eminence* (MGE) samples across multiple stages spanning peak neurogenesis, whereas the Polioudakis et al. (2019) dataset focuses on cells from the neocortex during mid-gestation (15–21 post-conception weeks). While the cell types profiled in the two datasets are related, they are not identical due to differences in the sampled tissue. This contrasts with the CITE-seq dataset considered previously, where training and test cells originated from the same source. This experiment

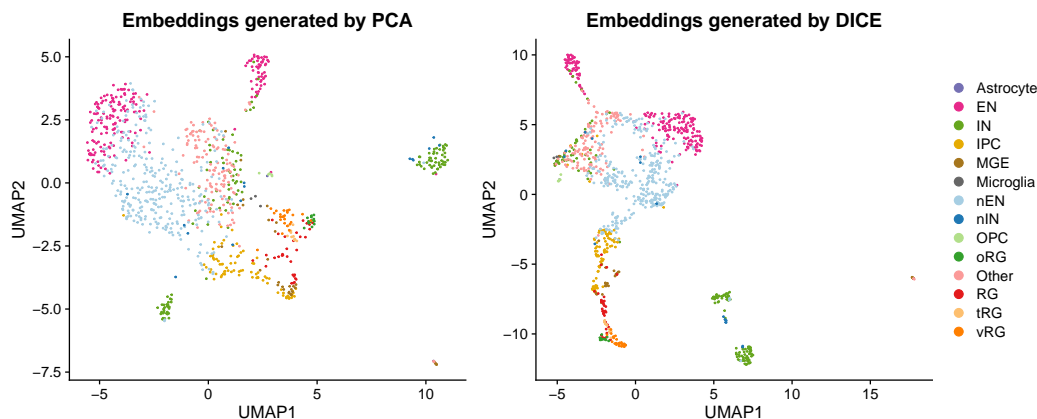


Figure 4: UMAP of 1,000 randomly sampled cells from the [Polioudakis et al. \(2019\)](#) dataset. Left: PCA embeddings in a 15-dimensional latent space using  $\hat{V}$  from the training set. Right: embeddings after denoising with DICE using a diffusion model trained on the [Nowakowski et al. \(2017\)](#) dataset.

evaluates the robustness of DICE to realistic distributional changes that occur during cross-dataset cell-type label transfer.

**Preprocessing and Denoising** We analyzed 3,495 cells from [Nowakowski et al. \(2017\)](#) and 15,126 cells from [Polioudakis et al. \(2019\)](#), both of which had undergone QC and transformations analogous to our CITE-seq workflow. Because the studies differ in protocols and development of the tissue under consideration, only 17,638 genes were shared; from this intersection we selected the top 5,000 highly variable genes, yielding matrices  $X_{\text{now}} \in \mathbb{R}^{3495 \times 5000}$  and  $X_{\text{pol}} \in \mathbb{R}^{15126 \times 5000}$ . Cell-type annotations were available only for the [Nowakowski et al. \(2017\)](#) data, so we performed label transfer to the [Polioudakis et al. \(2019\)](#) data using the Seurat v3 procedure ([Stuart et al., 2019](#)) over the shared genes. As  $X_{\text{now}}$  exhibited a stronger signal, we trained the diffusion prior on a  $k = 15$  latent projection of it (via PCA) and evaluated DICE on 1,000 randomly sampled cells from  $X_{\text{pol}}$  to assess denoising and embedding quality. The training and denoising hyperparameters (noise/annealing schedule, number of diffusion denoising steps, and number of Gibbs iterations) matched those used in the CITE-seq example.

**Evaluation** We compare UMAP visualizations for the embeddings constructed from the test data using DICE and the embeddings obtained via the PCA transform learned from the training data. Denoising substantially improves biological interpretability, with two salient gains. The canonical excitatory trajectory  $\text{RG} \rightarrow \text{IPC} \rightarrow \text{nEN} \rightarrow \text{EN}$  is visually continuous and easy to follow in the DICE embedding, whereas it appears fragmented under PCA. Further, the cluster of *inhibitory neurons* (IN) is also more compact and clearly separated after denoising, and DICE reveals a distinct branch emerging from IN in the test dataset that is largely masked in the PCA space. Finally, denoising cleanly separates *newborn inhibitory neurons* (nIN) from mature IN, highlighting developmental heterogeneity within the inhibitory lineage. Because [Nowakowski et al. \(2017\)](#) dataset is a smaller, high-signal reference spanning fewer cell types, while [Polioudakis et al. \(2019\)](#) dataset is a richer atlas, label transfer yields coarse annotations; consequently, global label-matching can penalize meaningful substructure. Indeed, ARI (using the same embedding clustering scheme as CITE-seq experiment) is 0.42 for PCA versus 0.35 for DICE, reflecting over-splitting of broad labels into finer, developmentally coherent groups in the test data. A locality-aware metric is more appropriate here: the cell-type LISI (Local Inverse Simpson’s Index ([Korsunsky et al., 2019](#)); lower is better for local purity) computed using the same clusters is markedly lower for DICE (7.27) than for PCA (8.25), indicating that denoising sharpens lineage relationships and resolves biologically relevant subpopulations that PCA tends to blur.

**Discussion** We introduced DICE, a latent plug-and-play framework for denoising and extracting meaningful embeddings from high-dimensional observational data with an underlying low-rank structure. Both synthetic and real-world experiments demonstrated its ability to denoise beyond the training distribution and the ability to leverage clean reference data for denoising. We further

showed that DICE can quantify uncertainty in cluster assignments and remains robust under model misspecification. Future work includes extending DICE beyond linear low-rank structures and the i.i.d. noise assumption, as well as improving the efficiency of the sampling procedure.

**Reproducibility statement** We provide the full codebase as supplementary material and will release it publicly upon publication. The appendix details the implementation, including hardware specifications, software packages, and training configurations. For synthetic experiments, we include both a description in the main text and code for data generation and preprocessing in the supplementary files. For real-world datasets, we describe dataset acquisition in the appendix, preprocessing steps in both the main text and appendix, and provide scripts to reproduce all experiments.

**Use of Large Language Models (LLMs)** Large Language Models (LLMs) were used to assist in preparing tables and figures and for proofreading.

**Acknowledgments** This work was supported in part by an AWS Cloud Credit Grant from Cornell’s Center for Data Science for Enterprise and Society.

## REFERENCES

- Ricard Argelaguet, Damien Arno, Danila Bredikhin, Yonatan Deloro, Britta Velten, John C. Marioni, and Oliver Stegle. Mofa+: a statistical framework for comprehensive integration of multi-modal single-cell data. *Genome Biology*, 21(1):111, 2020. doi: 10.1186/s13059-020-02015-1. URL <https://genomebiology.biomedcentral.com/articles/10.1186/s13059-020-02015-1>.
- Christopher JC Burges et al. Dimension reduction: A guided tour. *Foundations and Trends® in Machine Learning*, 2(4):275–365, 2010.
- Stanley H Chan, Xiran Wang, and Omar A Elgendy. Plug-and-play admm for image restoration: Fixed-point convergence and applications. *IEEE Transactions on Computational Imaging*, 3(1): 84–98, 2016.
- Alain Durmus, Éric Moulines, and Marcelo Pereyra. Efficient bayesian computation by proximal markov chain monte carlo: When langevin meets moreau. *SIAM Journal on Imaging Sciences*, 11(1):473–506, 2018.
- Rasa Elmentaite, Cristina Domínguez Conde, Lira Yang, and Sarah A. Teichmann. Single-cell atlases: shared and tissue-specific cell types across human organs. *Nature Reviews Genetics*, 23(6):395–410, 2022. doi: 10.1038/s41576-022-00449-w.
- Adam Gayoso, Romain Lopez, Zoë Steier, Jeffrey Regier, Aaron Streets, and Nir Yosef. A joint model of rna expression and surface protein abundance in single cells. *bioRxiv*, 2019. doi: 10.1101/791947. URL <https://www.biorxiv.org/content/early/2019/10/07/791947>.
- Andrew Gelman, John B. Carlin, Hal S. Stern, David B. Dunson, Aki Vehtari, and Donald B. Rubin. *Bayesian Data Analysis*. Chapman and Hall/CRC, Boca Raton, FL, 3rd edition, 2013. ISBN 978-1439840955.
- Hyojun Go, Yunsung Lee, Jin-Young Kim, Seunghyun Lee, Myeongho Jeong, Hyun Seung Lee, and Seungtaek Choi. Towards practical plug-and-play diffusion models. In *Proceedings of the IEEE/CVF conference on computer vision and pattern recognition*, pp. 1962–1971, 2023.
- Casper H. Grønbech, Malte F. Vording, Pascal N. Timshel, Casper Kaae Sønderby, Tune H. Pers, and Ole Winther. scvae: variational auto-encoders for single-cell gene expression data. *Bioinformatics*, 36(16):4415–4422, 2020. doi: 10.1093/bioinformatics/btaa293.
- Yuhan Hao, Stephanie Hao, Erica Andersen-Nissen, William M. Mauck, Shiwei Zheng, Andrew Butler, Maddie J. Lee, Aaron J. Wilk, Charlotte Darby, Matthew Zager, Paul Hoffman, Marlon Stoeckius, Efthymia Papalex, Eleni P. Mimitou, Jaison Jain, Arianne Srivastava, Tim Stuart,

- Lucas M. Fleming, Bertrand Yeung, Adam J. Rogers, Juliana M. McElrath, Catherine A. Blish, Raphael Gottardo, Peter Smibert, and Rahul Satija. Integrated analysis of multimodal single-cell data. *Cell*, 184(13):3573–3587.e29, 2021. doi: 10.1016/j.cell.2021.04.048.
- Jonathan Ho, Ajay Jain, and Pieter Abbeel. Denoising diffusion probabilistic models. *Advances in neural information processing systems*, 33:6840–6851, 2020.
- Lawrence Hubert and Phipps Arabie. Comparing partitions. *Journal of Classification*, 2(1):193–218, 1985. doi: 10.1007/BF01908075.
- Peter V. Kharchenko, Lev Silberstein, and David T. Scadden. Bayesian approach to single-cell differential expression analysis. *Nature Methods*, 11(7):740–742, 2014. doi: 10.1038/nmeth.2967.
- Vladimir Yu Kiselev, Tallulah S Andrews, and Martin Hemberg. Challenges in unsupervised clustering of single-cell rna-seq data. *Nature Reviews Genetics*, 20(5):273–282, 2019.
- Allon M Klein, Linas Mazutis, Ilke Akartuna, Naren Tallapragada, Adrian Veres, Victor Li, Leonid Peshkin, David A Weitz, and Marc W Kirschner. Droplet barcoding for single-cell transcriptomics applied to embryonic stem cells. *Cell*, 161(5):1187–1201, 2015.
- Ilya Korsunsky, Nghia Millard, Jean Fan, Kamil Slowikowski, Fan Zhang, Kevin Wei, Yury Baglaenko, Michael Brenner, Po-Ru Loh, and Soumya Raychaudhuri. Fast, sensitive and accurate integration of single-cell data with Harmony. *Nature Methods*, 16(12):1289–1296, 2019. doi: 10.1038/s41592-019-0619-0.
- Rik G. H. Lindeboom, Aviv Regev, and Sarah A. Teichmann. Towards a human cell atlas: taking notes from the past. *Trends in Genetics*, 37(7):625–630, 2021. doi: 10.1016/j.tig.2021.03.007.
- Romain Lopez, Jeffrey Regier, Michael B. Cole, Michael I. Jordan, and Nir Yosef. Deep generative modeling for single-cell transcriptomics. *Nature Methods*, 15(12):1053–1058, 2018. doi: 10.1038/s41592-018-0229-2.
- Erpai Luo, Minsheng Hao, Lei Wei, and Xuegong Zhang. scdiffusion: conditional generation of high-quality single-cell data using diffusion model. *Bioinformatics*, 40(9):btac518, 08 2024. ISSN 1367-4811. doi: 10.1093/bioinformatics/btac518. URL <https://doi.org/10.1093/bioinformatics/btac518>.
- Evan Z Macosko, Anindita Basu, Rahul Satija, James Nemesh, Karthik Shekhar, Melissa Goldman, Itay Tirosh, Allison R Bialas, Nolan Kamitaki, Emily M Martersteck, et al. Highly parallel genome-wide expression profiling of individual cells using nanoliter droplets. *Cell*, 161(5):1202–1214, 2015.
- Leland McInnes, John Healy, and James Melville. Umap: Uniform manifold approximation and projection. *arXiv preprint arXiv:1802.03426*, 2018.
- Leland McInnes, John Healy, Nathaniel Saul, and Lukas Grossberger. UMAP: Uniform manifold approximation and projection. *Journal of Open Source Software*, 5(48):228, 2020. doi: 10.21105/joss.02268.
- Ricardo J. Miragaia, Teresa Gomes, Anna Chomka, Laura Jardine, Anja Riedel, Ahmed N. Hegazy, Natasha Whibley, Alessia Tucci, Xueqing Chen, Ildiko Lindeman, Grace Emerton, Thomas Krausgruber, Jack Shields, Muzlifah Haniffa, Fiona Powrie, and Sarah A. Teichmann. Single-cell transcriptomics of regulatory t cells reveals trajectories of tissue adaptation. *Immunity*, 50(2):493–504.e7, 2019. doi: 10.1016/j.immuni.2019.01.001.
- Sagnik Nandy and Zongming Ma. Multimodal data integration and cross-modal querying via orchestrated approximate message passing, 2024.
- Tomasz J. Nowakowski, Aparna Bhaduri, Alex A. Pollen, Beatriz Alvarado, Mohammad A. Mostajo-Radji, Elizabeth Di Lullo, Maximilian Haeussler, Claudia Sandoval-Espinosa, Sophia J. Liu, Dmitry Velmeshev, Xian Wang, Daniel A. Lim, Joshua A. West, Anne Leyrat, W. James Kent, and Arnold R. Kriegstein. Spatiotemporal gene expression trajectories reveal developmental hierarchies of the human cortex. *Science*, 358(6368):1318–1323, 2017. doi: 10.1126/science.aap8809.

- Joshua Orvis et al. gear: Gene expression analysis resource portal for community-driven, multi-omic data exploration. *Nature Methods*, June 2021. doi: 10.1038/s41592-021-01200-9.
- Jae-Eun Park, Rachel A. Botting, Cristina Domínguez Conde, Diana-Maria Popescu, Marieke Lavaert, Daniel J. Kunz, Irene Goh, Emily Stephenson, Roberta Ragazzini, Elizabeth Tuck, Alice Wilbrey-Clark, Kimberley Roberts, Viktoria Kedlian, J. R. Ferdinand, Xiang He, Susan Webb, William M. Mauck, Roser Vento-Tormo, Krishna T. Mahbubani, Krzysztof Polanski, Zhichao Miao, Zewen Tuong, Pei He, Laura Jardine, Dale Taylor, Jan Engelbert, Mirjana Efremova, Miguel Vento-Tormo, Paolo Bonfanti, Helen King, Marianna Prete, Noam Rivlin, Adam Kurek, Ryan Tester, Steven Lisgo, David Henderson, Elena Prigmore, Daniela Amann-Zalcenstein, Itai Benhar, Ricardo J. Miragaia, Isabel Gomez-Tourino, John Fletcher, Simon Lindsay, Sam Behjati, Nigel R. Hardwick, Stuart Horswell, Krithika N. Natarajan, John Morton, Sarah Farnon, Sarah Miranda Lledó, Tina Moreau, George Wright, Ashley J. Waardenberg, Lennart Sontag, Emily Stephenson, Lyubov Mamanova, Jose Luis Sardina Ortega, Dimitrios A. Glinos, Johannes C. Melms, Marija Josipovic, and et al. A cell atlas of human thymic development defines t cell repertoire formation. *Science*, 367(6480):eaay3224, 2020. doi: 10.1126/science.aay3224.
- Adam Paszke, Sam Gross, Francisco Massa, Adam Lerer, James Bradbury, Gregory Chanan, Trevor Killeen, Zeming Lin, Natalia Gimelshein, Luca Antiga, Alban Desmaison, Andreas Köpf, Edward Yang, Zach DeVito, Martin Raison, Alykhan Tejani, Sasank Chilamkurthy, Benoit Steiner, Lu Fang, Junjie Bai, and Soumith Chintala. PyTorch: An imperative style, high-performance deep learning library. In *Proceedings of the 33rd International Conference on Neural Information Processing Systems*, volume 32 of *NeurIPS*, pp. 8026–8037. Curran Associates Inc., Red Hook, NY, USA, December 2019.
- Minshi Peng, Yue Li, Brie Wamsley, Yuting Wei, and Kathryn Roeder. Integration and transfer learning of single-cell transcriptomes via cfit. *Proceedings of the National Academy of Sciences*, 118(10):e2024383118, 2021. ISSN 0027-8424. doi: 10.1073/pnas.2024383118. URL <https://doi.org/10.1073/pnas.2024383118>.
- Simone Picelli, Åsa K Björklund, Omid R Faridani, Sven Sagasser, Gösta Winberg, and Rickard Sandberg. Smart-seq2 for sensitive full-length transcriptome profiling in single cells. *Nature methods*, 10(11):1096–1098, 2013.
- Simone Picelli, Omid R Faridani, Åsa K Björklund, Gösta Winberg, Sven Sagasser, and Rickard Sandberg. Full-length rna-seq from single cells using smart-seq2. *Nature protocols*, 9(1):171–181, 2014.
- Damon Polioudakis, Luis de la Torre-Ubieta, Jack Langerman, Ashley G. Elkins, Xiaowei Shi, Jason L. Stein, Christina K. Vuong, Stephan Nichterwitz, Maria Gevorgian, Christopher K. Opland, Dongxue Lu, William Connell, Elizabeth K. Ruzzo, James K. Lowe, Teodora Hadzic, Fiona I. Hinz, Samira Sabri, William E. Lowry, Mark B. Gerstein, Kathrin Plath, and Daniel H. Geschwind. A single-cell transcriptomic atlas of human neocortical development during mid-gestation. *Neuron*, 103(5):785–801.e8, 2019. doi: 10.1016/j.neuron.2019.06.011.
- Aviv Regev, Sarah A. Teichmann, Eric S. Lander, Ido Amit, Christophe Benoist, Ewan Birney, Bernd Bodenmiller, Peter Campbell, Piero Carninci, Menna Clatworthy, Hans Clevers, Bart Deplancke, Ian Dunham, James Eberwine, Roland Eils, Wolfgang Enard, Andy Farmer, Lars Fugger, Berthold Göttgens, Nir Hacohen, Muzlifah Haniffa, Martin Hemberg, Seung K. Kim, Paul Klennerman, Arnold Kriegstein, Ed Lein, Sten Linnarsson, Joakim Lundeberg, Partha P. Majumder, John C. Marioni, Miriam Merad, Musa Mhlanga, Martin Nawijn, Mihai Netea, Garry Nolan, Dana Pe’er, Anthony Phillipakis, Chris P. Ponting, Stephen Quake, Wolf Reik, Orit Rozenblatt-Rosen, Joshua R. Sanes, Rahul Satija, Ton N. Schumacher, Alex Shalek, Eytan Shapiro, Pramod Sharma, Jay W. Shin, Oliver Stegle, Michael Stratton, Michael J. T. Stubbington, Mathias Uhlen, Alexander van Oudenaarden, Allon Wagner, Fiona M. Watt, Irving Weissman, Barbara Wold, Ramnik Xavier, Nir Yosef, Julie Kent, Sean Sullivan, William R. Sellers, and Orit Rozenblatt-Rosen. The human cell atlas. *eLife*, 6:e27041, 2017. doi: 10.7554/eLife.27041.
- Gareth O. Roberts and Jeffrey S. Rosenthal. Optimal scaling of discrete approximations to langevin diffusions. *Journal of the Royal Statistical Society, Series B (Statistical Methodology)*, 60(1): 255–268, 1998. doi: 10.1111/1467-9868.00123.

- Peter J Rousseeuw. Silhouettes: a graphical aid to the interpretation and validation of cluster analysis. *Journal of Computational and Applied Mathematics*, 20:53–65, 1987.
- Ernest Ryu, Jialin Liu, Sicheng Wang, Xiaohan Chen, Zhangyang Wang, and Wotao Yin. Plug-and-play methods provably converge with properly trained denoisers. In *International Conference on Machine Learning*, pp. 5546–5557. PMLR, 2019.
- Uri Shaham, Kenneth P. Stanton, Jing Zhao, Hongyu Li, Khadir Raddassi, Ruth Montgomery, and Yuval Kluger. Removal of batch effects using distribution-matching residual networks. *Bioinformatics*, 33(16):2539–2546, 2017. doi: 10.1093/bioinformatics/btx196.
- Jascha Sohl-Dickstein, Eric Weiss, Niru Maheswaranathan, and Surya Ganguli. Deep unsupervised learning using nonequilibrium thermodynamics. In *International conference on machine learning*, pp. 2256–2265. pmlr, 2015.
- Jiaming Song, Chenlin Meng, and Stefano Ermon. Denoising diffusion implicit models. In *International Conference on Learning Representations*, 2021a.
- Yang Song, Jascha Sohl-Dickstein, Diederik P. Kingma, Abhishek Kumar, Stefano Ermon, and Ben Poole. Score-based generative modeling through stochastic differential equations. In *International Conference on Learning Representations (ICLR)*, 2021b.
- Tim Stuart, Andrew Butler, Paul Hoffman, Christoph Hafemeister, Efthymia Papalexi, William M. Mauck, Yuhao Hao, Marlon Stoeckius, Peter Smibert, and Rahul Satija. Comprehensive integration of single-cell data. *Cell*, 177(7):1888–1902.e21, 2019. doi: 10.1016/j.cell.2019.05.031.
- Singanallur V Venkatakrishnan, Charles A Bouman, and Brendt Wohlberg. Plug-and-play priors for model based reconstruction. In *2013 IEEE global conference on signal and information processing*, pp. 945–948. IEEE, 2013a.
- Swaminathan V. Venkatakrishnan, Charles A. Bouman, and Brendt Wohlberg. Plug-and-play priors for model based reconstruction. In *IEEE Global Conference on Signal and Information Processing (GlobalSIP)*, pp. 945–948, 2013b. doi: 10.1109/GlobalSIP.2013.6737048.
- Allon Wagner, Aviv Regev, and Nir Yosef. Revealing the vectors of cellular identity with single-cell genomics. *Nature Biotechnology*, 34(11):1145–1160, 2016. doi: 10.1038/nbt.3711.
- Wenjie Wang, Xin Zhang, Fei Yu, Chen Wang, Yi Zhang, Xin Liu, and Tong Xu. cfdiffusion: conditional diffusion model with caching mechanism for single-cell rna-seq data generation. *Briefings in Bioinformatics*, 26(1):bbaf071, 2025. doi: 10.1093/bib/bbaf071.
- Yufei Wang, Ming Luo, Chenyu Chen, Jun Wu, and Guanghui Zhang. stdiff: A diffusion model for spatial transcriptomics data imputation. *Briefings in Bioinformatics*, 25(3):bbae171, 2024. doi: 10.1093/bib/bbae171.
- Eric Weine, Peter Carbonetto, and Matthew Stephens. Accelerated dimensionality reduction of single-cell rna sequencing data with fastglm-pca. *Bioinformatics*, 40(8):btae494, 08 2024. ISSN 1367-4811. doi: 10.1093/bioinformatics/btae494. URL <https://doi.org/10.1093/bioinformatics/btae494>.
- Zihui Wu, Yu Sun, Yifan Chen, Bingliang Zhang, Yisong Yue, and Katherine Bouman. Principled probabilistic imaging using diffusion models as plug-and-play priors. In *The Thirty-eighth Annual Conference on Neural Information Processing Systems*, 2024. URL <https://openreview.net/forum?id=Xq9HQf7VNV>.
- Xingyu Xu and Yuejie Chi. Provably robust score-based diffusion posterior sampling for plug-and-play image reconstruction. In *Advances in Neural Information Processing Systems (NeurIPS)*, 2024. URL [https://proceedings.neurips.cc/paper\\_files/paper/2024/file/3fa2d2b637122007845a2fbb7c21453b-Paper-Conference.pdf](https://proceedings.neurips.cc/paper_files/paper/2024/file/3fa2d2b637122007845a2fbb7c21453b-Paper-Conference.pdf).
- Heng Zhang, Chen Li, Rui Zhou, and Tao Wang. Lapddpm: Laplacian-guided diffusion probabilistic model for single-cell rna-seq data generation. *arXiv preprint*, arXiv:2506.13344, 2025. URL <https://arxiv.org/abs/2506.13344>.

Hongyi Zhang, Moustapha Cisse, Yann N Dauphin, and David Lopez-Paz. mixup: Beyond empirical risk minimization. In *International Conference on Learning Representations*, 2018.

Kai Zhang, Yawei Li, Wangmeng Zuo, Lei Zhang, Luc Van Gool, and Radu Timofte. Plug-and-play image restoration with deep denoiser prior. *IEEE Transactions on Pattern Analysis and Machine Intelligence*, 44(10):6360–6376, 2021.

Xinyi Zhong, Chang Su, and Zhou Fan. Empirical bayes pca in high dimensions. *Journal of the Royal Statistical Society: Series B*, 84(3):853–878, 2022. doi: 10.1111/rssb.12490.

Yuanzhi Zhu, Kai Zhang, Jingyun Liang, Jiezhong Cao, Bihan Wen, Radu Timofte, and Luc Van Gool. Denoising diffusion models for plug-and-play image restoration. In *IEEE Conference on Computer Vision and Pattern Recognition Workshops (NTIRE)*, 2023.

## A DIFFUSION TRAINING

For a given noise schedule  $\{\alpha_t\}_{t \in [T]}$ , noisy versions of  $\widehat{U}_i^{(r)}$  are generated as

$$\widehat{U}_{t,i}^{(r)} = \sqrt{\bar{\alpha}_t} \widehat{U}_i + \sqrt{1 - \bar{\alpha}_t} \varepsilon_{t,i}, \quad \varepsilon_{t,i} \stackrel{\text{i.i.d.}}{\sim} \mathcal{N}_k(0, I_k), \quad (8)$$

where  $\bar{\alpha}_t = \prod_{s=1}^t \alpha_s$ . A neural network  $\widehat{\varepsilon}_{\theta_t}(\widehat{U}_{t,i}^{(r)}; t)$  is trained to predict the injected noise  $\varepsilon_{t,i}$  from the corrupted sample  $\widehat{U}_{t,i}^{(r)}$  by minimizing the mean-squared error

$$\mathcal{L}(\theta) = \frac{1}{m} \sum_{i=1}^m \|\varepsilon_{t,i} - \widehat{\varepsilon}_{\theta}(\widehat{U}_{t,i}^{(r)}; t)\|_2^2.$$

The fitted network provides an estimate of  $\mathbb{E}[\varepsilon_{t,i} \mid \widehat{U}_{t,i}^{(r)}]$ , which is directly related to the score function of the marginal distribution  $p_t(\widehat{U}_{t,i}^{(r)})$  via

$$\nabla_{\widehat{U}_{t,i}^{(r)}} \log p_t(\widehat{U}_{t,i}^{(r)}) \approx -\frac{1}{\sqrt{1-\bar{\alpha}_t}} \widehat{\varepsilon}_{\theta}(\widehat{U}_{t,i}^{(r)}; t).$$

Thus, training the model to predict noise is equivalent to estimating the score function, which in turn defines the reverse diffusion process and enables sampling from the prior  $P_{\text{prior}}$ . For the detailed procedure, see Algorithm 2.

## B PROOF OF PROPOSITION 3.1

To prove Proposition 3.1 let us observe that if  $f(\cdot)$  is the density of standard multivariate Gaussian distribution, then

$$f(X_i - VZ_i) = \frac{1}{(2\pi)^{d/2}} \exp\left(-\frac{1}{2}\|X_i - VZ_i\|_2^2\right).$$

Therefore

$$P_{\rho}(Z_q^{(s)} \mid X_q, U_q) \propto \exp\left(-\frac{1}{2}\|X_q - \widehat{V}Z_q^{(s)}\|_2^2 - \frac{1}{2\rho_s^2}\|U_q^{(s)} - Z_q^{(s)}\|_2^2\right) \quad (9)$$

$$\stackrel{(1)}{\propto} \exp\left(-\frac{1}{2}(Z_q^{(s)})^\top \left(\frac{1}{\rho_s^2}I_k + \widehat{V}^\top \widehat{V}\right) Z_q^{(s)} + (Z_q^{(s)})^\top \left(\widehat{V}^\top X_q + \frac{1}{\rho_s^2}U_q^{(s)}\right)\right) \quad (10)$$

$$\stackrel{(2)}{\propto} \exp\left(-\frac{1}{2}(Z_q - m_q)\Lambda^{-1}(Z_q - m_q)\right), \quad (11)$$

where

$$\Lambda = \left(\frac{1}{\rho_s^2}I_k + \widehat{V}^\top \widehat{V}\right)^{-1} \quad (12)$$

$$m_q = \Lambda \left(\widehat{V}^\top X_q + \frac{1}{\rho_s^2}U_q^{(s)}\right), \quad (13)$$

and (2) follows by completing the quadratic form in the power of the exponential in (1) to match the density of a Gaussian distribution. Then the proposition follows by identifying the density on the right-hand side of (2) as that of a Gaussian distribution with mean  $m_q$  and covariance  $\Gamma$ .

---

**Algorithm 2** Train diffusion model

---

**Require:** Training set  $\{X_i^{(r)}\}_{i \in [T]}$ , epochs  $E$ , noise schedule  $\{\alpha_t\}_{t \in [T]}$ , embedding dimension  $k$

**Ensure:** Trained model  $\hat{\varepsilon}_\theta$

- 1: Calculate the factor loading matrix  $\hat{V}$  from the training data by projecting  $X^{(r)}$  to a  $k$  dimensional latent space using PCA.
- 2: Compute  $\hat{U}_i = \hat{V}^\top X_i^{(r)}$ .
- 3: **for**  $e = 1, \dots, E$  **do**
- 4:   Independently sample timestep  $t^{(i)} \sim \mathcal{U}\{1, \dots, T\}$  for all  $i = 1, \dots, m$
- 5:   Draw noises  $\varepsilon_{t^{(i)}, i} \sim \mathcal{N}(0, 1)$  for all  $i$
- 6:   Construct noised inputs

$$\hat{U}_{t,i}^{(r)} = \sqrt{\bar{\alpha}_{t^{(i)}}} \hat{U}_i + \sqrt{1 - \bar{\alpha}_{t^{(i)}}} \varepsilon_{t^{(i)}, i}, \quad \text{for } i = 1, \dots, m,$$

- and  $\bar{\alpha}_{t^{(i)}} = \prod_{s=1}^{t^{(i)}} \alpha_s$
- 7:   Compute loss

$$\mathcal{L}(\theta) = \frac{1}{m} \sum_{i=1}^m \|\varepsilon_{t,i} - \varepsilon_\theta(\hat{U}_{t,i}^{(r)}, t^{(i)})\|_2^2$$

- 8:   Take gradient step on  $\theta$ .
  - 9: **end for**
  - 10: **return**  $\varepsilon_\theta$
- 

## C MODEL ARCHITECTURE AND IMPLEMENTATION DETAILS FOR TRAINING THE DIFFUSION MODELS USED IN THE SINGLE CELL EXPERIMENTS

**Overview** Across all experiments, we use the same denoising network, `TabularDiffusionMLP`, which predicts Gaussian noise  $\varepsilon_{t,i}$  from the noised sample  $\hat{U}_{t,i}^r \in \mathbb{R}^k$  at diffusion step  $t$ . The architecture is parameterized by the number of residual MLP blocks  $M$  and the hidden dimension  $D$ . For synthetic experiments, we use a smaller model with  $M = 2$  blocks and hidden dimension  $D = 64$  ( $\approx 150,000$  trainable parameters), trained for  $E = 2,000$  epochs. For single-cell experiments, we employ a larger model with  $M = 8$  blocks and hidden dimension  $D = 512$  ( $\approx 35,000,000$  trainable parameters), trained for  $E = 20,000$  epochs. We use a batch size of  $B = 4048$  across all models.

**Input encoders** We encode the data and the diffusion time with separate branches: (i) a linear projection  $U_t^r \mapsto \mathbb{R}^D$ , and (ii) a sinusoidal positional embedding of  $t$  followed by two SiLU-activated linear layers to  $\mathbb{R}^D$ . We then concatenate the two  $D$ -dimensional features into a  $2D$ -dimensional vector.

**Backbone** The concatenated features are processed by eight residual MLP blocks of constant width  $2D$ . Each block expands to  $4D$  units and contracts back to  $2D$  (Linear  $2D \rightarrow 4D$ , BatchNorm1d, SiLU, Linear  $4D \rightarrow 2D$ , BatchNorm1d), and adds a residual skip connection. This design provides sufficient capacity while remaining simple and fast for tabular inputs.

**Output head** A final projection (Linear  $2D \rightarrow D$ , SiLU, Linear  $D \rightarrow d$ ) produces  $\varepsilon_\theta(\hat{U}_t^{(r)}, t)$  in the same dimensionality as  $\hat{U}_t^{(r)}$ .

**Training objective and schedule** We adopt the standard noise-prediction loss  $\mathcal{L}(\theta)$  defined in Algorithm 2 with a linear  $\beta$  schedule:  $\beta_t \in [10^{-4}, 2 \times 10^{-2}]$  linearly spaced over  $T = 512$  steps and  $\alpha_t = 1 - \beta_t$ ,  $\bar{\alpha}_t = \prod_{s=1}^t \alpha_s$ . We optimize with AdamW (learning rate  $1 \times 10^{-4}$ , batch size 4048) for 20000 epochs.

**Data augmentation in training** High-quality single-cell datasets may contain relatively few cells but provide reliable labels. We leverage these labels for data augmentation during diffusion model training. Inspired by *mixup* by Zhang et al. (2018), we interpolate between multiple same-class samples rather than mixing across classes. Concretely, given a sample  $X_i^{(r)}$  with label  $Y_i^{(r)}$ , we select four additional same-class points and construct

$$\tilde{X}_i^{(r)} = \sum_{j=1}^5 \lambda_j x_j, \quad (\lambda_1, \dots, \lambda_5) \sim \text{Dirichlet}(1).$$

During training, we select the interpolated version  $\tilde{X}_i^{(r)}$  with a probability of  $p = 0.9$ . This intra-class mixup enriches the training distribution and improves robustness for the single-cell data. We use no data augmentation for the synthetic experiments.

**Layer specification** For completeness, Table 2 lists the exact layers and tensor shapes ( $B$  denotes batch size).

Stage	Operation / Activation	Output shape
<i>Input projections</i>		
$\hat{U}_t^{(r)}$ branch	Linear ( $k \rightarrow D$ )	$(B, D)$
$t$ embedding	Sinusoidal ( $1 \rightarrow 16$ )	$(B, 16)$
	Linear ( $16 \rightarrow D$ ) + SiLU	$(B, D)$
	Linear ( $D \rightarrow D$ ) + SiLU	$(B, D)$
CONCAT	—	$(B, 4D)$
<i>Residual MLP block (repeated <math>\times M</math>)</i>		
Hidden	Linear ( $2D \rightarrow 4D$ )	$(B, 4D)$
	BatchNorm1d ( $4D$ ), SiLU	$(B, 4D)$
	Linear ( $4D \rightarrow 2D$ )	$(B, 2D)$
	BatchNorm1d ( $2D$ )	$(B, 2D)$
Residual	$x \leftarrow x + \text{block}(x)$	$(B, 2D)$
<i>Output projection</i>		
Head	Linear ( $2D \rightarrow D$ ) + SiLU	$(B, D)$
	Linear ( $D \rightarrow k$ )	$(B, k)$

Table 2: Layer specification for `TabularDiffusionMLP` predicting  $\varepsilon_\theta(\hat{U}_t^{(r)}, t)$ .  $B$  is batch size,  $k$  is the input (latent) dimension,  $D$  is the hidden dimension of the network

**Practical notes** We normalize  $t$  to  $[0, 1]$  prior to sinusoidal embedding, use SiLU activations throughout, BatchNorm1d within blocks, and default PyTorch initializations.

**Implementation setup** We implemented all experiments in Python. Neural network training was performed in PyTorch (Paszke et al., 2019) on GPU-accelerated hardware, using a mix of AWS `g4dn.xlarge` EC2 instances and a dedicated Ubuntu server with an NVIDIA GeForce GTX 1070 (8GB RAM).

**Runtime** The runtime of our method can be divided into training and inference. Training is dominated by parameter updates for the diffusion model, with speed depending on hardware and chosen model size. Using the CITE-seq setup as an example, training on 9,000 cells with 3,000 dimensions for 10,000 epochs required approximately 11 hours on the EC2 instance.

Inference proceeds via Gibbs sampling, alternating between the prior and likelihood steps. The prior step, which involves sampling from the diffusion model, is the most computationally expensive. As  $\rho$  determines the starting timestep of the diffusion model  $t$ , the duration of the prior sampling is dependent on  $\rho$ , larger values of  $\rho$  result in longer runtime. For example, one Gibbs iteration on 1,000 test cells takes about 30 seconds for  $\rho = 1$ , corresponding to roughly 30 minutes of total runtime for denoising the test set of the CITE-seq dataset with 100 Gibbs iterations.

## D DISCUSSION ON THE CLUSTERING METRICS

To assess the quality of clustering in the learned embeddings, we employ three complementary metrics: the average cosine silhouette score (Rousseeuw, 1987), the Adjusted Rand Index (ARI) (Hubert & Arabie, 1985), and the cell-type Locally Invariant Simpson Index (cLISI) (Korsunsky et al., 2019). Below, we provide a brief description of each metric.

1. **Average Cosine Silhouette Score.** The silhouette score quantifies how well a point is matched to its assigned cluster compared to other clusters, measured here using cosine distance. For a point  $i$ , let  $a(i)$  denote the average intra-cluster cosine distance, and let  $b(i)$  denote the minimum average cosine distance between  $i$  and any other cluster. The silhouette score for  $i$  is defined as

$$s(i) = \frac{b(i) - a(i)}{\max\{a(i), b(i)\}}.$$

We report the mean silhouette score across all points as a global measure of clustering quality, with values closer to 1 indicating more distinct and coherent clusters.

2. **Adjusted Rand Index (ARI).** The Rand Index evaluates the agreement between two partitions by counting the proportion of point pairs that are consistently assigned together or apart. The ARI corrects this measure for chance, making it more robust in settings with many clusters. It is defined as

$$\text{ARI} = \frac{\text{RI} - \mathbb{E}[\text{RI}]}{\max(\text{RI}) - \mathbb{E}[\text{RI}]},$$

where RI is the raw Rand Index and  $\mathbb{E}[\text{RI}]$  is the expected value of the number of agreeing pairs under random clustering but fixed cluster sizes. ARI values range from 0 (chance-level agreement) to 1 (perfect alignment with ground truth).

3. **Cell-type Locally Invariant Simpson Index (cLISI).** The Local Inverse Simpson’s Index (LISI) was originally introduced to assess batch mixing in single-cell integration tasks. We adapt it to clustering by replacing batch labels with cluster (or cell-type) labels, yielding cLISI. For each cell  $i$ , cLISI measures the effective number of distinct clusters represented in its  $k$ -nearest neighbor neighborhood:

$$\text{LISI}(i) = \left( \sum_c p_{ic}^2 \right)^{-1},$$

where  $p_{ic}$  is the fraction of neighbors of  $i$  belonging to cluster  $c$ . We report the average cLISI across all cells. Lower values correspond to locally purer clusters, while higher values indicate greater mixing. Unlike ARI, cLISI does not require ground truth annotations and provides a local measure that complements the global silhouette score.

## E ABLATION STUDIES ON THE ROLE OF $\rho$

DICE employs a split Gibbs sampling scheme that introduces an auxiliary variable  $Z_i$  to decouple the likelihood and prior updates. The strength of the coupling between  $Z_i$  and  $U_i$  is controlled through the Gaussian alignment penalty

$$-\frac{1}{2\rho^2} \|U_i - Z_i\|_2^2, \tag{14}$$

which appears in both the likelihood and prior steps (see Equation 5 and Equation 6). Intuitively,  $\rho$  controls the distance between the sampling of  $U_i$  and  $Z_i$  in both the likelihood and prior step.

To interpret the role of  $\rho$ , we start by reviewing the canonical inverse problem of denoising: we observe a noisy matrix  $X$ , and our goal is to recover a clean, underlying matrix  $UV^\top$ , where  $U$  is unknown. This problem is naturally framed in a Bayesian setting. The likelihood  $f(X - UV^\top | U)$ , models the noise process, while the prior  $P_{\text{prior}}(U)$  encodes our assumptions about the structure of

$U$ . A standard approach is to find the *Maximum a Posterior* (MAP) estimate, which solves the optimization problem:

$$\hat{U}_{\text{MAP}} = \arg \min_U \underbrace{-\log f(X - UV^\top | U)}_{\ell(U; X)} - \underbrace{\log P_{\text{prior}}(U)}_{R(U)},$$

where  $\ell(U; X)$  is the data-fidelity term, and  $R(U)$  is the regularizer induced by the prior. While this yields a single point estimate, it discards all uncertainty about the solution.

To capture the full posterior distribution, we turn to *posterior sampling*, targeting:

$$\pi(U | X) \propto f(X - UV^\top | U) P_{\text{prior}}(U).$$

This problem can be viewed as a *soft relaxation* of the MAP problem. The key is to observe that sampling from this posterior can be efficiently achieved using a Split Gibbs Sampler. (Xu & Chi, 2024; Venkatakrishnan et al., 2013b).

The sampler introduces an auxiliary variable  $Z$  and iterates between two conditional sampling steps:

1. **Data-consistency Step (likelihood step):** Sample  $Z$  from  $p(Z | U, X)$ , which typically involves the likelihood  $f$  and projects information from the observation  $X$  and the current state  $U$ .
2. **Prior-projection Step (prior step):** Sample  $U$  from  $p(U | Z) \propto P_{\text{prior}}(U) \cdot \delta(U \approx Z)$ . This critical step draws a sample from the prior distribution that is consistent with the auxiliary variable  $Z$ .

As we repeat this sampling procedure, the two steps eventually reach a stochastic equilibrium. When  $\rho$  is small, the strong coupling term dominates both steps. In this regime:

- The initialization (typically from the data distribution as in Algorithm 1) has a persistent influence because the strong coupling prevents substantial deviation from previous states.
- Both the likelihood and prior terms become relatively less influential compared to the alignment constraint.
- The sampler produces outputs that remain close to the initialization throughout the sampling process.

When  $\rho$  is large, the coupling is weak, allowing:

- The prior term to dominate the U-update step, pulling samples toward the prior distribution.
- The data likelihood to have more influence in the Z-update step.
- Greater exploration away from the initialization.

Overall,  $\rho$  controls the trade-off between fidelity to the observation and adherence to the learned prior. Small  $\rho$  enforces tight coupling and rapid convergence near the data distribution, while large  $\rho$  allows freer interaction between the two updates and greater influence of the prior. In the following experiments, we empirically investigate how varying  $\rho$  affects the resulting embeddings when (i) applying DICE repeatedly to the same input observation (subsection E.1), and (ii) when the clusters present in the test data differ from those seen during training (subsection E.2).

## E.1 SPREAD ACROSS RUNS

**Setup** To assess the sensitivity of DICE to different values of  $\rho$ , we perform an ablation study by denoising a fixed input point multiple times and comparing the spread across runs. By fixing the input observation to a single point, we can isolate the effect of  $\rho$  on the variability introduced by the stochastic sampling procedure. We use the two-cluster setup (see section 4, Setup 1), and use the same input point for all runs, the center of Cluster 2. We generate 500 independent runs of DICE for  $\rho \in [0.1, 0.5, 1.0, 5.0, 10.0, 20.0]$ .

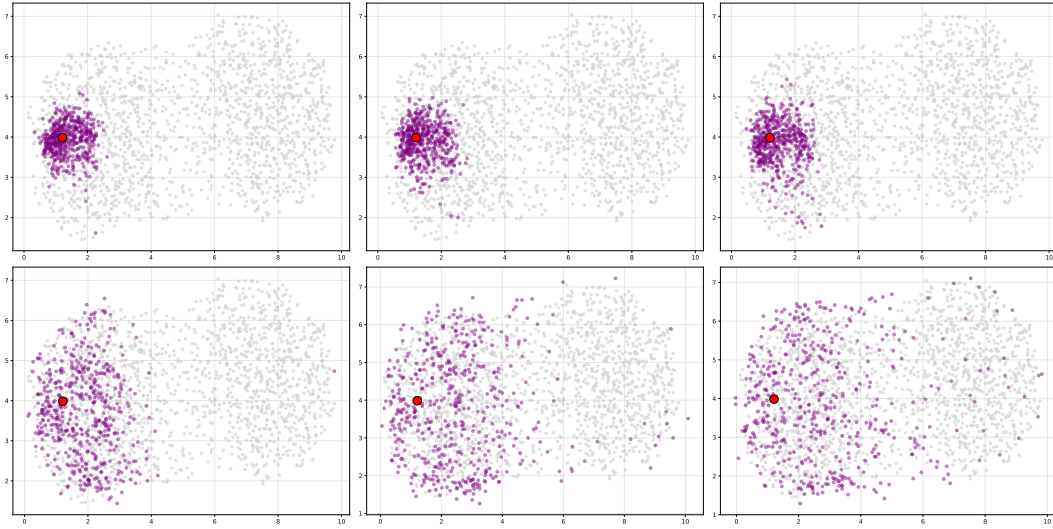


Figure 5: UMAP visualizations of 500 runs of DICE-denoised embeddings for the Cluster 2 center under Setup 1 with increasing  $\rho \in [0.1, 0.5, 1.0, 5.0, 10.0, 20.0]$  (left to right, top to bottom). Input observation in red; training data in grey.

**Results** We visualize the generated embeddings under different values of  $\rho$  with a UMAP in Figure 5. As  $\rho$  increases, the spread of the sampled points grows: for small  $\rho$ , points remain tightly concentrated around the cluster center, while for large  $\rho$ , they disperse more broadly. The spread of the sampled points can be interpreted as the posterior uncertainty under different assumed noise levels. When the assumed noise is low (small  $\rho$ ), the posterior is sharply concentrated around the observation, as the likelihood dominates and little deviation from the measurement is plausible. In contrast, for higher noise levels (large  $\rho$ ), the posterior becomes broader, reflecting greater uncertainty: a wider range of latent points is consistent with the observed data. Thus, varying  $\rho$  calibrates how strongly the likelihood influences the denoised embedding.

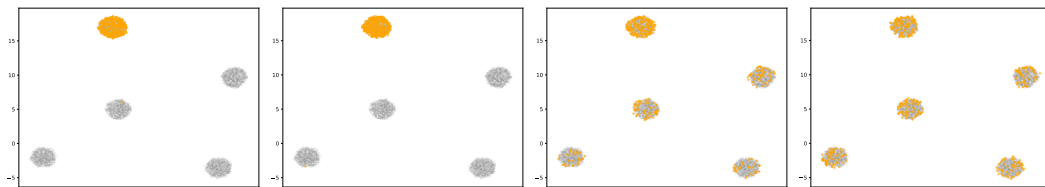


Figure 6: UMAP visualizations of PCA projections (left) and DICE-denoised embeddings for test points restricted to a single cluster, with increasing values of  $\rho \in [1.0, 8.0, 20.0]$  (left to right). As  $\rho$  increases, the embeddings gradually shift from being measurement-aligned to prior-aligned. Training data are shown in grey.

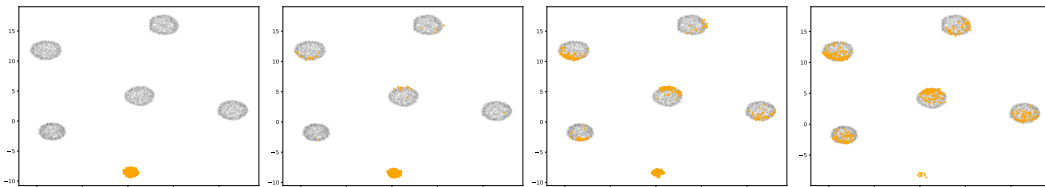


Figure 7: UMAP visualizations PCA projections (left) and DICE-denoised embeddings for test points from a cluster *not observed during training*, shown for increasing  $\rho \in [0.5, 2.0, 4.0]$  (left to right). With larger  $\rho$ , the unseen cluster progressively gets mapped to the training clusters, reflecting stronger prior alignment. Training data are shown in grey. The UMAP projection is fitted jointly on the combined training and test data.

## E.2 MISMATCH BETWEEN TRAINING AND TEST CLUSTERS

In this section, we investigate the influence of prior guidance under different  $\rho$ . We create a mismatch between the training and the test data, and evaluate whether points stay close to the measurement, or are moved according to the prior. We update our training data fixed to contain 5 well separated clusters. Then, we vary the input test data, which either comes only from one cluster, or from a new cluster which is not present in the training data. Our diffusion model is the same as for the other synthetic experiments (see [Appendix C](#)). We run DICE for 200 Gibbs iterations without averaging, and report results for different choices of  $\rho$ .

**Training data** We extend our synthetic data generation to include five instead of two cluster centers, while still following the same low-rank latent structure. We chose low noise levels, such that the training data is well separated. In detail, we start by drawing the cluster centers  $\mu_i \sim \mathcal{N}_{15}(0, I_{15})$  in latent dimension  $k = 15$ . The training prior is a balanced Gaussian mixture,  $P_{\text{prior}} = \sum_i \frac{1}{5} \mathcal{N}_{15}(\mu_i, 0.3 I_{15})$  with each component corresponding to one cell type. We sample a loading matrix  $V \in \mathbb{R}^{200 \times 15}$  with entries i.i.d.  $\mathcal{N}(0, 1)$ . For each cell  $i$ , we draw a latent  $U_i^{(r)} \sim P_{\text{prior}}$  and measurement noise  $\varepsilon_i^{(r)} \sim \mathcal{N}_{200}(0, 0.5 I_{200})$ , and generate a synthetic expression profile  $X_i^{(r)} = V U_i^{(r)} + \varepsilon_i^{(r)} \in \mathbb{R}^{200}$ ,  $i = 1, \dots, 8000$ . This yields a training dataset  $\mathcal{D}^{(r)}$  of size  $m = 8,000$  in  $d = 200$  observed dimensions. We generate a test dataset  $\mathcal{D}^{(t)}$  of size  $m = 2,000$  by increasing the noise variance  $\varepsilon_i^{(t)} \sim \mathcal{N}_{200}(0, I_{200})$ .

### E.2.1 FEWER CLUSTERS IN THE TRAINING DATA

**Setup** We construct a test set consisting solely of cells from a single cluster. This setup corresponds to a mismatch where the model’s learned prior encompasses a richer structure than what is present in the observed data: While DICE is trained on a uniform distribution across clusters, where each cluster is equally likely, the test data only contains one cluster.

**Results** We plot the PCA projection (left), and generated denoised embeddings for  $\rho \in [1.0, 8.0, 20.0]$  (left to right) in [Figure 6](#). DICE projects all samples into one of the learned clusters, independent of  $\rho$ . However,  $\rho$  controls which of the learned clusters the observations are assigned to. For small  $\rho$ , samples remain close to their noisy measurements, resulting in all embeddings staying in the original input cluster. For intermediate  $\rho$ , most points concentrate within one cluster, but a subset diffuses into neighboring clusters. For large  $\rho$ , the denoising process aligns closely with the prior, resulting in approximately uniform assignment across clusters, independent of the original observation.

### E.2.2 MORE CLUSTERS IN THE TRAINING DATA

**Setup** We now consider the opposite case, where the test data includes a new cluster that was unseen during training. Specifically, we sample an additional cluster center  $\mu_i$  from the same generative process as in the main setup, ensuring that this cluster lies outside the support of the training data.

**Results** We show a UMAP visualization of PCA projection (left), and generated denoised embeddings for  $\rho \in [0.5, 2.0, 4.0]$  in [Figure 7](#). To observe the test cluster, the UMAP is fitted jointly on the combined training and test data. The PCA projection (left) shows that test measurements form a new cluster, which is non-overlapping with the initial training clusters plotted in gray. For small  $\rho$ , DICE maintains a distinct cluster of points around the novel cluster. As  $\rho$  increases, samples gradually disperse into the nearest training clusters, reflecting the influence of the prior. With  $\rho = 4.0$ , almost all points are assigned to clusters from the training set. Notably, even for large  $\rho$ , the measurements still exert a directional influence on the embedding. Points are not assigned uniformly inside the clusters, but tend to align with parts of the clusters more consistent with the observed input.

## E.3 DISCUSSION

The results obtained by varying  $\rho$  highlight the trade-off between data fidelity and prior alignment. A small  $\rho$  keeps denoised samples close to their observations, preserving local variations even when

they deviate from the training data. In contrast, a large  $\rho$  guides samples toward representations consistent with the learned prior. This ability to steer between these regimes makes  $\rho$  a powerful control parameter for balancing embedding quality across datasets of differing noise levels. When the data are assumed to be low-noise, a small  $\rho$  maintains proximity to the measurements, allowing structure not captured in the training set to emerge. Conversely, for high-noise data, a larger  $\rho$  leverages the prior to guide the estimates toward more reliable, denoised representations.

## F DATA SOURCES

**CITE-seq benchmark.** We used the *Seurat v4 CITE-seq* dataset distributed with `scvi-tools` as our atlas building benchmark. The original Seurat object and feature matrices were taken directly from the `scvi` example and used without modification, except for preprocessing and downsampling steps described in Section 5.

**Human fetal brain development.** We analyzed two fetal neocortex transcriptomic datasets, [Nowakowski et al. \(2017\)](#) and [Polioudakis et al. \(2019\)](#), obtained via the [gEAR \(Gene Expression Analysis Resource\)](#) portal ([Orvis et al., 2021](#)). For both studies, we downloaded the author-provided processed count matrices and accompanying metadata from gEAR and restricted analyses to the shared gene set as detailed in Section 5.

**Provenance and licensing.** All datasets were used under the terms specified by their original authors and hosting platforms. We performed only secondary analysis; no new data were generated for this work.